Power Research - A Journal of CPRI, Vol 22(1), 2026 | pp. 45-55

Experimental Demonstration of Virtual Inertia of Battery Energy Storage Fed Grid-Forming Inverter

Amit Kumar Pal*, Biswajit Acharya and Samir Hazra

Department of Electrical Engineering, Indian Institute of Science, Bengaluru, India; kpamit@iisc.ac.in

Keywords: BESS, Grid-forming Inverter, RoCoF, Virtual Inertia

Article Received: 18-01-2026
Article Revised: 10-02-2026
Article Accepted: 19-02-2026

DOI: 10.33686/pwj.22.1.2026.45-55

*Author for Correspondence

Abstract

Grid-forming inverters are becoming an essential component of modern power systems as the penetration of renewable energy sources increases. They play a critical role in providing frequency and voltage stability in low-inertia grids. Battery energy storage systems (BESS), equipped with grid-forming inverters, can enhance local grid strength and provide inertial support during sudden power imbalances. This capability can be achieved by emulating synchronous machine behavior through a control approach known as the Virtual Synchronous Generator (VSG). This paper presents a grid-forming control design based on the Virtual Synchronous Generator (VSG) concept. The design includes the voltage control loop and a systematic procedure for selecting virtual inertia and damping parameters derived from established control guidelines. The proposed control strategy is experimentally validated on a 20 kW hardware setup. Experimental results demonstrate accurate active power reference tracking and effective inertial response under grid frequency disturbances with different Rates of Change of Frequency (RoCoF).

This is an open access article under the terms of the **CC BY:** Allows others to copy, distribute, and build upon the work for any purpose, provided they credit the original creator

© 2026 The Author(s). *Central Power Research Institute* published by Informatics Publishing Limited

1. INTRODUCTION

Modern power grids are experiencing large-scale integration of Inverter-Based Resources (IBRs), fundamentally transforming power system design and operation. This transition has significant implications for inverter control strategies and overall system stability. Traditionally, IBRs have been operated as grid-following inverters that rely on a strong grid for synchronization and reference generation. However, with the declining contribution of synchronous generators and the resulting reduction in system inertia, present-day power systems increasingly require IBRs to actively support the grid by providing voltage regulation and frequency stability.

Grid-forming inverters operate as controlled voltage sources behind an impedance and can regulate grid voltage and frequency without relying on external synchronization. Among various grid-forming strategies, the Virtual Synchronous Generator (VSG) concept has attracted considerable attention due to its ability to emulate the inertial and droop characteristics of synchronous machines through control algorithms. By embedding the swing equation into the active power control loop, VSG-based inverters can provide virtual inertia and damping, thereby contributing to improved frequency stability during power imbalances and grid disturbances.

Battery Energy Storage Systems (BESS) equipped with grid-forming inverters have emerged as an effective platform for implementing VSG-based control due to their fast response capability and bidirectional power flow. Recent studies have shown that grid-forming BESS can significantly improve system frequency stability by reducing the Rate of Change of Frequency (RoCoF) and supporting the frequency nadir following disturbances. Unlike synchronous machines, BESS-based inverters do not face mechanical constraints, allowing virtual inertia and damping parameters to be flexibly tuned while achieving faster and more controllable dynamic responses. Consequently, grid-forming BESS are increasingly deployed for renewable integration support, microgrid operation, black-start capability, and system strength enhancement in low-inertia power systems[1]. Furthermore, prior comparative studies have shown that conventional droop-controlled inverters lack inertial behavior, leading to higher RoCoF during grid disturbances. In contrast, VSG-based control introduces inertia through the swing equation, thereby improving transient frequency response while maintaining comparable steady-state performance[2].

This work focuses on the practical implementation and experimental validation of VSG-based grid-forming control for BESS applications. For grids with highly inductive source impedance and a Short-Circuit Ratio (SCR) greater than 10, the small-signal dynamics can be assumed weakly dependent on the operating point. Under this condition, the active and reactive power control loops can be effectively decoupled during VSG implementation[3]. Based on these established principles, this paper implements a VSG-based grid-forming control scheme and validates its inertial response experimentally.

2. GRID FORMING CONTROL WITH VIRTUAL INERTIA

2.1 Voltage Control Implementation

Figure 1 illustrates the per-phase linear model of the inverter and grid used for voltage control design. The inverter is represented as a controlled voltage source v_{inv}. The output filter is an LCL configuration consisting

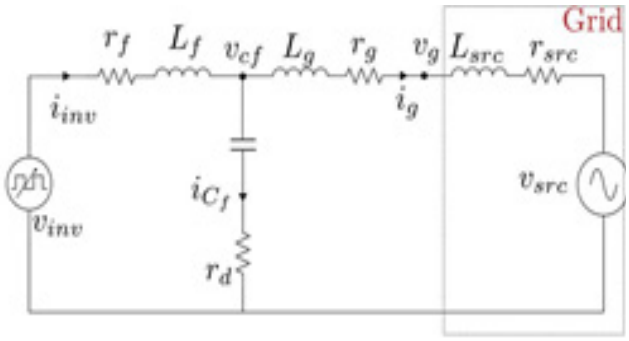


Figure 1. Per-phase linear model of the inverter and grid used as the plant for voltage controller design.

of an inverter-side inductor L_f with resistance L_f, a grid-side inductor L_g with resistance L_g, and a filter capacitor C_f with damping resistance L_d. The grid is modeled as a voltage source v_{src} behind an equivalent impedance composed of an inductance L_{srcand} resistance r_{src}.

The three-phase variables are transformed into space vectors using the definition.

$$\mathbf{x} = \frac{2}{3}\left(x_a + x_b e^{j2\pi/3} + x_c e^{j4\pi/3}\right)$$

Based on this representation, the dynamic vector equations of the system are given as follows.

$$L_f \frac{d\mathbf{i_{inv}}}{dt} = \mathbf{v_{inv}} - \mathbf{v_{cf}} - r_f \mathbf{i_{inv}} \quad (1)$$

$$\left(L_g + L_{src}\right)\frac{d\mathbf{i_g}}{dt} = \mathbf{v_{cf}} - \mathbf{v_{src}} - \left(r_g + r_{src}\right)\mathbf{i_g} \quad (2)$$

$$C_f \frac{d\mathbf{v_{cf}}}{dt} = \frac{r_d C_f}{L_f}\mathbf{v_{inv}} + \frac{r_d C_f}{L_g + L_{src}}\mathbf{v_{src}} + \mathbf{i_{inv}} - \mathbf{i_g}$$

$$-r_d C_f \left(\frac{1}{L_f} + \frac{1}{L_g + L_{src}}\right)\mathbf{v_{cf}} \quad (3)$$

$$v_g = v_{cf} - L_g \frac{di_g}{dt} - r_{gi_g} \quad (4)$$

where $L_{\text{tot}} = L_g + L_{\text{src}}$ and $r_{\text{tot}} = r_g + r_{\text{src}}$.

Transforming (1)–(4) into the synchronous -reference frame yields the state space model x˙=Ax +Bu andy=Cx+ Du, with state vector x, input vector u and output vector y matrices are as follows:

$$\text{x} = \left[v_{cd}, v_{cq}, i_{id}, i_{iq}, i_{gd}, i_{gq}\right]^T,$$

$$\text{u} = \left[v_{invd}, v_{invq}, v_{srcd}, v_{srcq}\right]^T, \text{y} = \left[v_{gd}, v_{gq}\right]^T.$$

$$A = \begin{bmatrix} a_1 & \omega & a_2 & 0 & -a_2 & 0 \\ -\omega & a_1 & 0 & a_2 & 0 & -a_2 \\ -a_3 & 0 & a_4 & \omega & 0 & 0 \\ 0 & -a_3 & -\omega & a_4 & 0 & 0 \\ a_5 & 0 & 0 & 0 & a_6 & \omega \\ 0 & a_5 & 0 & 0 & -\omega & a_6 \end{bmatrix} \quad (5)$$

$$B = \begin{bmatrix} b_1 & 0 & b_2 & 0 \\ 0 & b_1 & 0 & b_2 \\ a_3 & 0 & 0 & 0 \\ 0 & a_3 & 0 & 0 \\ 0 & 0 & -a_5 & 0 \\ 0 & 0 & 0 & -a_5 \end{bmatrix} \quad (6)$$

$$C = \begin{bmatrix} c_1 & 0 & 0 & 0 & c_2 & 0 \\ 0 & c_1 & 0 & 0 & 0 & c_2 \end{bmatrix} \quad (7)$$

$$D = \begin{bmatrix} 0 & 0 & d_1 & 0 \\ 0 & 0 & 0 & d_1 \end{bmatrix} \quad (8)$$

The coefficients for the state-space matrices are given as,

$$a_1 = -r_d\left(\frac{1}{L_f} + \frac{1}{L_{tot}}\right), a_2 = \frac{1}{C_f}, a_3 = \frac{1}{L_f}$$

$$a_4 = -\frac{r_f}{L_f}, a_5 = \frac{1}{L_{tot}}, a_6 = -\frac{r_{tot}}{L_{tot}}$$

$$b_1 = \frac{r_d}{L_f}, b_2 = \frac{r_d}{L_{tot}}$$

$$c_1 = 1 - \frac{L_g}{L_{tot}}, c_2 = \frac{L_g r_{tot}}{L_{tot}} - r_g, d_1 = \frac{L_g}{L_{tot}}$$

The derived state-space formulation is utilized for the design of the inner voltage PI controller to ensure accurate PCC voltage tracking and robust disturbance rejection. In the -domain, the linear model maps the inverter control inputs and grid disturbances to the PCC voltage as:

$$\boldsymbol{Y}(s) = [C(sI - A)^{-1}B + D]\boldsymbol{U}(s) \quad (9)$$

By extracting the corresponding transfer functions from $v_{inv,dq}$ to $v_{g,dq}$, frequency-domain bode analysis is performed to design the PI controller gains for the desired bandwidth and phase margin. Simultaneously, the disturbance transfer functions relating grid source voltage fluctuations v_{srcto} the PCC voltage v_g are obtained, allowing for the integration of disturbance rejection into the control design.

The LCL filter parameters and the damping resistance play a critical role in shaping the system

dynamics and in providing sufficient passive damping to suppress filter resonance. A detailed analysis of LCL filter design and the selection of damping resistors for grid-connected inverter applications is presented in[4].

2.2 Virtual Inertia Emulation

In a synchronous machine, the rotor dynamics are represented by the swing equation given in (10). The rotor acceleration is governed by the net torque acting on the shaft, which includes the mechanical torque T_m applied to the rotor, the electromagnetic torque T_e generated due to the interaction between the rotor field and the stator magnetic field, and the damping torque T_d. The damping torque is primarily produced by the damper windings and is proportional to the speed deviation between the rotor speed and the synchronous speed dictated by the grid frequency.

$$J\dot{\omega} = T_m - T_e - T_d \tag{10}$$

In (10), J represents the rotor inertia. A higher inertia limits the rate of change of angular frequency $\dot{\omega}$, thereby reducing the Rate of Change of Frequency (RoCoF). A slower frequency deviation provides a larger time window for control and protection actions to respond to grid disturbances, which ultimately contributes to improved system stability.

By multiplying both sides of (10) by the nominal angular frequency ω_0, the swing equation can be expressed in power form as given in (11), where $M = J\omega_0$ represents the angular momentum of the rotor. In (11), P_m and $P_{edenote}$ the mechanical input power and the electromagnetic output power, respectively. The damping torque T_d, which is proportional to $(\omega-\omega_0)$, $T_d\ \omega_0$ can be represented using an equivalent damping coefficient D, as $D(\omega-\omega_0)$. Defining the frequency deviation as $\Delta\omega = \omega-\omega_0$, the swing equation can be rewritten in the compact form shown in (12).

$$M\dot{\omega} = P_m - P_e - D(\omega - \omega_0) \tag{11}$$

$$M\Delta\dot{\omega} = P_m - P_e - D\Delta\omega \tag{12}$$

The inertia of a synchronous machine is commonly characterized by the inertia constant H, which is defined as the ratio of the kinetic energy stored in the rotor at nominal speed to the rated apparent power of the machine. The inertia parameter M, which represents the inertia of the machine in the swing equation, can be related to the inertia constant H through the rated apparent power S_{base} shown in (14).

$$H = \frac{\frac{1}{2}J\omega_0^2}{S_{base}} \tag{13}$$

$$M = \frac{2H \times S_{base}}{\omega_0} \tag{14}$$

Equation (12) is used to emulate the inertia behavior of a synchronous machine in a grid-forming inverter, where the mechanical power P_{mis} replaced by a power reference P_{ref}. By implementing the swing equation in the power synchronization loop, the Virtual Synchronous Generator (VSG) enables the inverter to exhibit inertia-like frequency behavior similar to that of a synchronous machine. In contrast, conventional droop-based synchronization does not provide true inertial response and therefore cannot inherently limit the initial RoCoF. The use of virtual inertia in the VSG helps limit RoCoF and improves the frequency response during grid disturbances.

2.3 Linearized VSG Model and Parameter Selection

The power synchronization loop of a grid-forming inverter is inherently nonlinear. Developing a small-signal model for parameter selection therefore requires linearization around a specific operating point, which complicates the design process. In this work, the focus is on studying the initial-stage inertial response; hence, a simplified system representation is adopted. It is assumed that the grid is sufficiently strong and predominantly inductive, such that the power transfer angle , defined as the phase angle between the inverter

voltage and the grid voltage, remains small. Under this condition, the nonlinear power transfer relationship can be linearized.

With these assumptions, the active power transfer between the inverter and the grid can be expressed as,

$$P = \frac{3V_g V_{src}}{X_{src}} \sin(\delta) \quad (15)$$

where V_{ga} nd V_{srcare} the RMS values of the grid voltage and the inverter voltage, respectively, and X_{src} represents the equivalent grid-side reactance. For small power angles (e.g., $\delta<5°$), the approximation $\sin(\delta) \approx \delta$ introduces negligible errors, and the power equation can be linearized as,

$$P \approx \frac{3V_g V_{src}}{X_{src}} \delta \quad (16)$$

Since the inverter is operated close to nominal conditions, the inverter voltage magnitude is assumed to be approximately equal to the grid voltage i.e.,

$$V_{base} \approx V_g \approx V_{src}$$

By equating the power transfer expression to the rated power,

$$\frac{3V_g V_{src}}{X_{src}} \delta = 3V_{base} I_{base}$$

which simplifies to,

$$\frac{X_{src} I_{base}}{V_{base}} = \delta$$

Thus, the per-unit grid reactance is denoted by $X_{src,pu}$, and the Short-Circuit Ratio (SCR) can be approximated as,

$$SCR = \frac{1}{X_{src,pu}}$$

For small power angles ($\delta<5°$), this approximation remains valid. Under the considered system parameters, this condition results in SCR>10. As reported in 3, an SCR greater than 10 ensures effective decoupling between the active and reactive power control loops, thereby justifying the *P*–*Q* decoupling assumption adopted in this study.

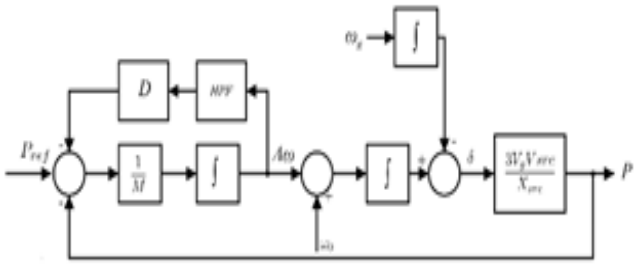


Figure 2. Block diagram of the linearized active power control loop.

Using (12) and (16), a linearized model of the power synchronization loop is obtained. Figure 2 shows the block diagram of the resulting linearized VSG-based control structure. In this diagram, the inner voltage control loop, which regulates the voltage magnitude and phase angle references, is omitted. Since the bandwidth of the inner voltage control loop is significantly higher than that of the power synchronization loop, it is assumed to have unity gain within the frequency range of interest for the power loop.

Here ω_g represents the grid voltage source frequency and acts as a disturbance input to the power synchronization model. The nominal grid frequency ω_0 is obtained during grid connection using phase-locked loop (PLL) synchronization. Once the VSG mode is activated, ω_0 is kept constant and serves as the nominal frequency for the virtual inertia implementation. To ensure proper steady-state power tracking while providing damping during transients, a High-Pass Filter (HPF) is applied to the frequency deviation $\Delta\omega$ in the damping path.

Once the small-signal model of the power loop is obtained, the remaining task is the selection of the virtual inertia Mand damping coefficient D. For clarity of analysis, the high-pass filter in the damping path is temporarily neglected, and the intrinsic power–frequency control loop is analyzed. The small-signal

open-loop gain L(s) of the power control loop can be expressed as,

$$L(s) = \frac{3V_g V_{src}}{X_{src}} \cdot \frac{1}{M} \cdot \frac{1}{s + \frac{D}{M}} \cdot \frac{1}{s} \quad (17)$$

The resulting closed-loop dynamics can be mapped to a standard second-order underdamped system with complex conjugate poles, characterized by the natural frequency ω_n and damping ratio ζ[5].

$$\mathrm{L}(s) = \frac{\omega_n^2}{s(s + 2\zeta\omega_n)}$$

From direct comparison, the natural frequency and damping ratio are obtained as,

$$\omega_n^2 = \frac{K_p}{M} \quad (18)$$

$$2\zeta\omega_n = \frac{D}{M} \quad (19)$$

Where, $K_p = \frac{3V_g V_{src}}{X_{src}}$

For an underdamped second-order system, the phase margin is related to the damping ratio by,

$$\mathrm{PM} = \tan^{-1}\left(\frac{2\zeta}{\sqrt{1 - 2\zeta^2}}\right)$$

and the closed-loop bandwidth can be approximated as,

$$\omega_b \approx 1.5\,\omega_n\sqrt{1 - 2\zeta^2} \quad (20)$$

Accordingly, the parameters M and D can be systematically selected to satisfy specified bandwidth and phase-margin requirements.The inclusion of a High-Pass Filter (HPF) in the damping path is required to ensure accurate steady-state tracking of the active power reference. This requirement can be explained by analyzing the disturbance transfer function between

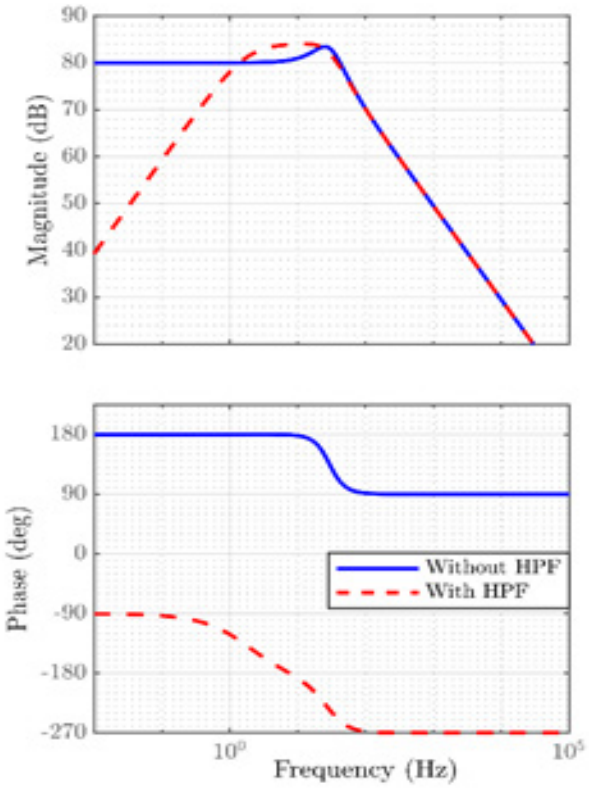


Figure 3. Bode plot of transfer function Gd(s) with and without high-pass filter (HPF).

the grid frequency disturbance ω_g and the inverter output power, whose frequency-domain behavior is illustrated in Figure 3. The corresponding disturbance transfer function is given by:

$$G_d(s) = \frac{P(s)}{\omega_g(s)} = -\frac{K_p}{s} \cdot \frac{1}{1 + L(s)} \quad (21)$$

In the absence of the HPF, the disturbance transfer function exhibits a finite DC gain. As a result, when the grid frequency ω_g deviates from the nominal frequency ω_0, a steady-state offset is introduced in the active power output, preventing accurate tracking of the power reference. This behavior is evident from the frequency-domain response, where the low-frequency gain remains non-zero for the system without the HPF.

With the inclusion of the HPF, the DC gain of the disturbance transfer function is effectively attenuated, eliminating the steady-state power offset. At the same time, the sensitivity of the active power to grid frequency variations is preserved over the relevant frequency range. This characteristic is desirable for inertia emulation, as it enables the inverter to inject or absorb power in response to frequency changes while maintaining correct steady-state power tracking.

3. EXPERIMENTAL SETUP

For experimental verification of the proposed virtual inertia–based grid-forming control, a laboratory-scale test setup is implemented consisting of a bidirectional dc power supply, a two-level SiC inverter built in our lab, and a programmable grid emulator. The experimental setup is shown in Figure 4. The grid impedance in the setup is determined by the transformer leakage

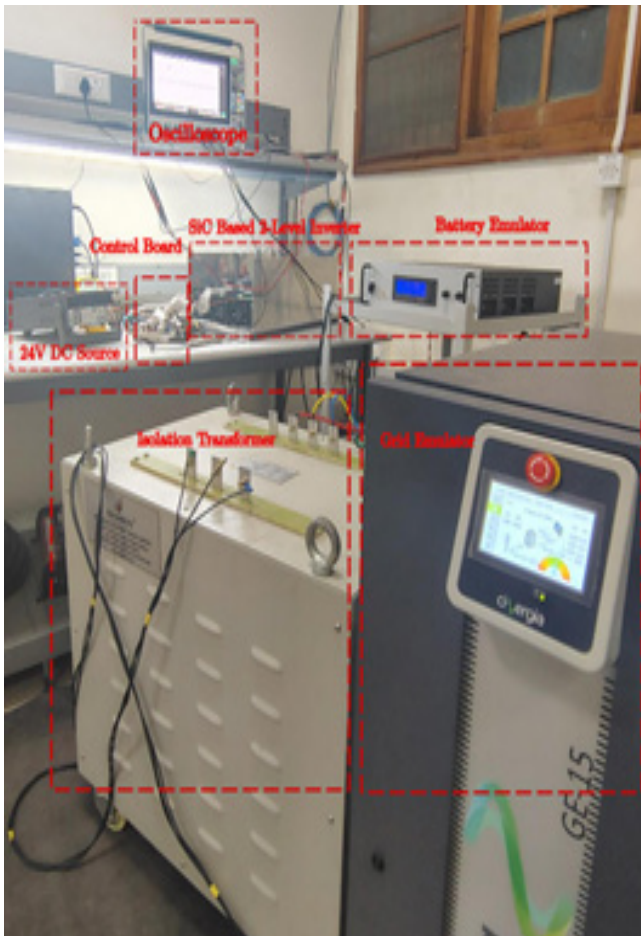


Figure 4. Bode plot of transfer function Gd(s) with and without high-pass filter (HPF).

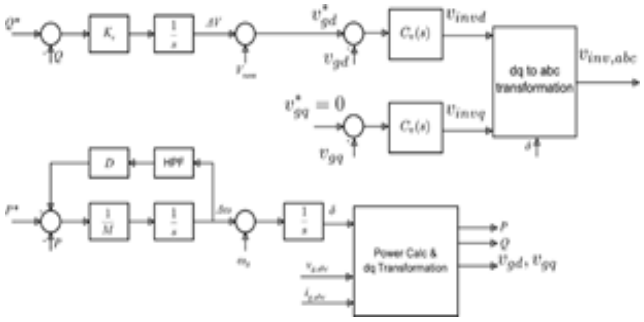


Figure 5. Block diagram of the virtual synchronous generator (VSG)–based grid-forming (GFM) control implemented in the experimental setup.

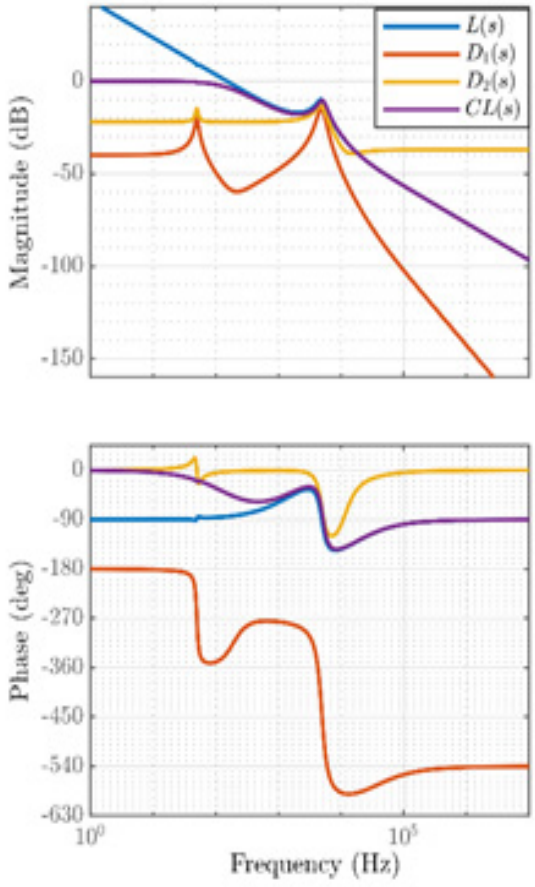


Figure 6. Bode plot of the closed-loop inner voltage control system using C_v (s) = K_p+K_i /s with K_p = 0.1 and K_i = 1025.

inductance between the grid emulator and the inverter and is represented by the equivalent source inductance L_{src}.

The main experimental parameters are as follows: a dc bus voltage of 750 V, grid emulator voltage of 230 $V_{ph,rms}$ at 50 Hz, inverter rated power of 20 kW, switching frequency of 40 kHz, and source inductance L_{src} = 270" " µH.

Figure 5 shows the block diagram of the Virtual Synchronous Generator (VSG)–based grid-forming control implemented in the experimental setup. The control structure consists of an inner voltage control loop operating in the synchronous reference frame and an outer power synchronization loop based on the swing equation. The VSG generates frequency and phase-angle reference according to the active power imbalance, while the Point-of-Common-Coupling (PCC) voltage reference is adjusted based on reactive power imbalance. The inner voltage controller regulates the inverter output voltage to track the reference generated by the VSG. The bandwidth of the inner voltage control loop is designed to be significantly higher than that of the power synchronization loop, allowing the voltage dynamics to be considered instantaneous from the perspective of inertial response.

The inner voltage controller employs a proportional–integral (PI) structure. The closed-loop frequency response of the voltage control loop, shown in Figure 6, exhibits a bandwidth of approximately 150 Hz and a phase margin of about 90°. In this figure, the loop gain is defined as $L(s)=C_v$ (s) v_{gd} s/$v_{inv,d}$ (s), while $D_1(s)=v_{gd}$ (s)/v_q(s) and D_2 (s)=v_{gd} (s)/$v_{src,d}$ (s) represent the disturbance transfer functions. The closed-loop response is given by CL(s)=L(s)/(1+L(s)). Furthermore, the disturbance-rejection responses discussed in Section 2.1 can be leveraged to improve robustness by appropriately augmenting the PI controller.

The objective of this work is not an in-depth optimization of the inner voltage controller design. Instead, the primary focus is on experimental validation of the inertial response characteristics of the grid-forming inverter. Special attention is required in designing the inner voltage controller because it directly affects harmonic reduction and determines interaction between the inner control loop and outer VSG dynamics, which in turn influences the overall voltage regulation performance[7].

Typical inertia constants reported for synchronous machines range from approximately 2 s to 10 s [6]. Accordingly, a representative inertia constant of H≈2.0s is selected in this study to emulate the behaviour of a 20 kW synchronous generator. The corresponding virtual inertia and damping parameters are chosen as M=250 Js\/rad and D=21000 J\/rad, respectively, for a desired damping ratio of ζ=0.5.

In addition, due to power rating limitations of the experimental setup during high rate-of-change-of-frequency (RoCoF) testing, a reduced inertia case is also considered for comparison. In this case, an inertia constant of H ≈ 0.5s is assumed, resulting in parameter values of M = 55 Js/rad and D=10000 J/rad.

The reactive power control loop can be designed using a similar approach. In this work, the reactive power gain k_v shown in Figure 5 is selected as k_v = 0.0051[3].

Experimental tests are conducted to evaluate active power reference tracking for a 5 kW step change, as well as the response of the system to grid frequency disturbances. Frequency deviations of 0.1 Hz are applied with RoCoF values of 0.2 Hz/s, 0.5 Hz/s, and 1.0 Hz/s to assess the inertial and damping performance of the proposed grid-forming control.

The High-Pass Filter (HPF) used for steady-state tracking is defined as follows. The lower cutoff frequency ω_1 is selected to ensure a reasonable tracking speed; however, an appropriate choice of ω_1 requires further investigation of the power-loop dynamics, which needs further investigation. The upper cutoff frequency ω_2 is constrained by the DSP interrupt service routine (ISR) cycle time. The study is carried out for ω_1=10 rad\/sand ω_2 =10000 rad\/s.

$$\mathrm{HPF}(s) = \frac{1.414\,\omega_2 s}{s^2 + (\omega_1 + \omega_2)s + \omega_1\omega_2}$$

4. RESULTS AND DISCUSSION

With the selected control parameters, the inverter is initially connected to the grid at zero active power reference. A step change of 5 kW in the active power reference is then applied. For M = 250 Js/radand D=21000 J/rad, corresponding active power and phase current responses are shown in Figure 7. A well-damped second-order response is observed, confirming stable dynamics of the Virtual Synchronous Generator (VSG)–based grid-forming control. Reference tracking is achieved, without steady-state error, demonstrating the effectiveness of the proposed VSG implementation.

The inertial response of the system is evaluated under grid frequency disturbances. Figure 8 shows the simulated response of the disturbance transfer function G_d (s) for a RoCoF of 0.5 Hz/s. To validate the analytical and simulation results, similar frequency disturbance tests are conducted on the experimental hardware setup. The corresponding frequency deviation responses Δω are recorded and compared with the simulation results.

The experiments are performed for two different virtual inertia values while maintaining the same damping ratio (ζ=0.5). A grid frequency disturbance with a RoCoF of 0.5 Hz/s and a total frequency drop of 0.1 Hz is applied. The results show that a higher virtual inertia constant H leads to a slower frequency response, indicating delayed synchronization with the grid frequency. Furthermore, once the RoCoF event ends, the system with higher inertia exhibits a longer settling time, consistent with inertial behavior.

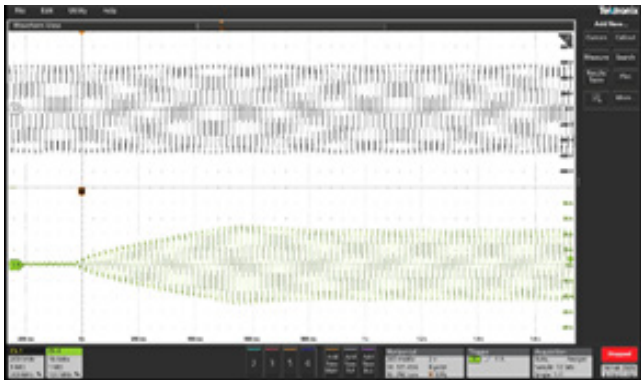


Figure 7. Experimental active power and phase-current responses for a 5 kW step change in the power reference (H = 2 s, ζ = 0.5). Ch 1 shows the line-to-line voltage, and Ch 4 shows the line current.

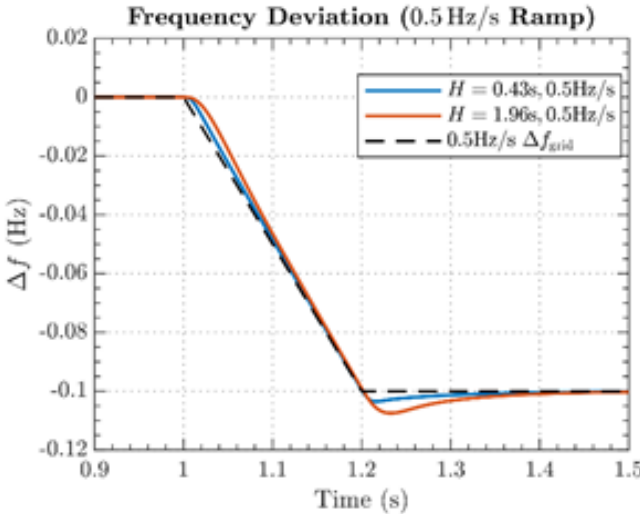


Figure 8. Simulated inertial response using the disturbance transfer function G_d (s) for H = 0.43 s and H = 1.96 s under a grid RoCoF of 0.5 Hz/s.

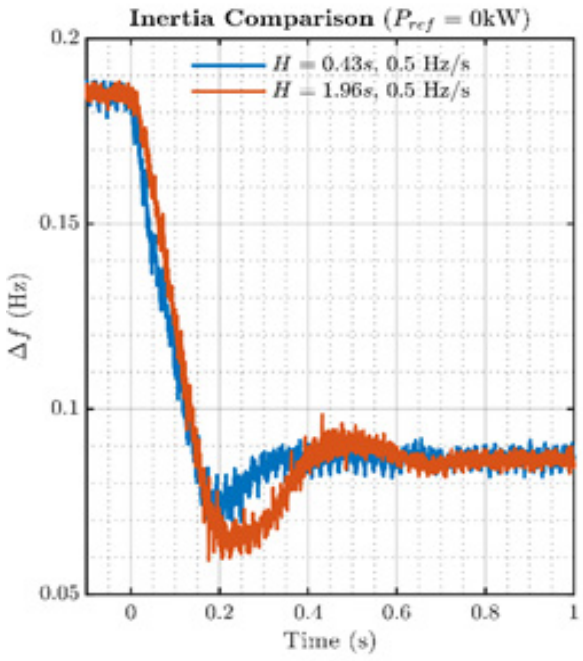


Figure 9. Experimental frequency response for H=0.43 s and H = 1.96 s under a grid RoCoF of 0.5 Hz/s.

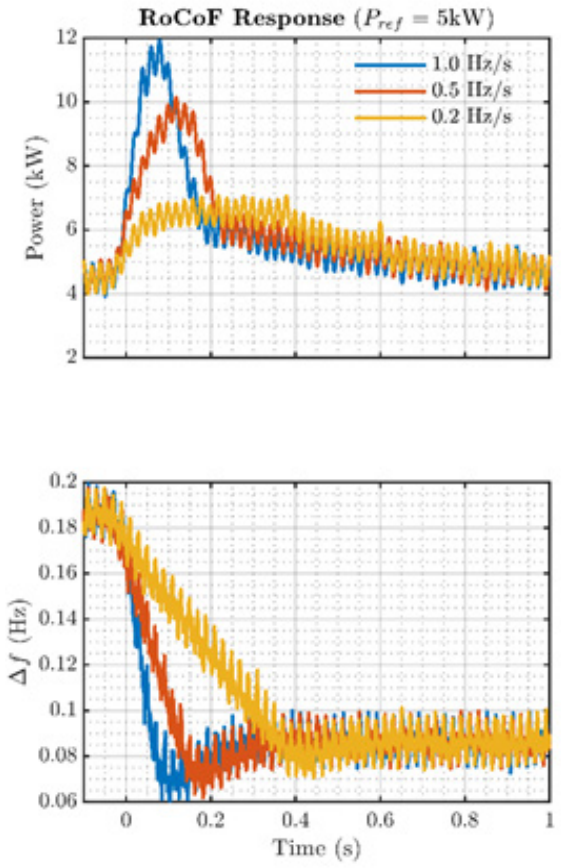


Figure 10. Experimental results of inverter power and frequence response to different grid RoCoF for H = 0.43 s.

Figure 8 and 9 demonstrate close agreement between the simulation and experimental results, thereby validating the proposed model and control implementation. The observed frequency dynamics confirm the presence of virtual inertia, as opposed to a pure droop-based response, which would react instantaneously to grid frequency disturbances.

Another experiment is conducted to evaluate the reserve power required to implement a specified virtual inertia for a given grid RoCoF. In this test, the virtual inertia is set to H≈0.5 w ith a damping ratio of ζ = 0.5, while the RoCoF is varied from 0.2 to 1 Hz/s. The corresponding peak active power drawn from the BESS is measured.

Although simulation results are not presented for this case, the developed linear model accurately estimates the observed peak power demand. This validates the applicability of the proposed model for reserve power estimation and BESS sizing. The experimental results are shown in Figure 10.

In the results, active power is calculated using measured line-to-line voltages V_{ab} and V_{bc}, along with phase currents I_a and I_c, employing the oscilloscope's internal math function. The frequency deviation Δω is an internal control variable within the digital controller and is obtained through a digital-to-analog converter (DAC) output. An external low-pass filter is used to remove high-frequency noise from the DAC signal before plotting.

5. CONCLUSION

This paper presented a virtual inertia–based grid-forming control strategy for BESS inverters using a VSG implementation that embeds the swing equation within the power synchronization loop. The role of a high-pass filter in the damping path was highlighted to ensure accurate steady-state active power tracking while preserving inertial response to grid frequency disturbances. Experimental results from a laboratory-scale setup demonstrated effective active power tracking and distinct inertial behaviour under different RoCoF conditions, providing practical insight into the trade-off between virtual inertia levels, inertial power requirements, and BESS/inverter rating constraints in low-inertia power systems.

In this work, the emulated inertia primarily shapes the inverter's frequency dynamics during grid disturbances through controlled power absorption or injection, rather than directly compensating system-level power imbalance. Extending the proposed framework to provide grid-level inertia support would require power-imbalance–driven control, dedicated experimental infrastructure, and careful system-level design, and is therefore beyond the scope of the present study.

6. ACKNOWLEDGEMENT

The authors would like to thank the Anusandhan National Research Foundation (ANRF) for financial support of this research under Grant No. ANRF/ECRG/2024/004701.

7. REFERENCES

1. Denholm P, Nunemaker J, Cooley J, O'Connell M, Brinkman G. Inertia and the power grid: a guide without the spin. Golden (CO): National Renewable Energy Laboratory (NREL); 2020. Report No.: NREL/TP-6A20-73856.
2. Liu J, Y, Ise T. Comparison of dynamic characteristics between virtual synchronous generator and droop control in inverter-based distributed generators. IEEE Trans Power Electron. 2016; 31(5):3600-3611. https://doi.org/10.1109/TPEL.2015.2465852
3. Wu H, Wang X, Blaabjerg F. Small-signal modelling and parameter design for virtual synchronous generators. IEEE Trans Ind Electron. 2016; 63(7):4292-4303. https://doi.org/10.1109/TIE.2016.2543181
4. Acharya B, Pal AK, Hazra S. A comprehensive approach to LCL filter design for high-switching-frequency inverters connected to weak grids. IEEE Energy Conversion Congress & Exposition Asia (ECCE-Asia), Bengaluru, India; 2025. https://doi.org/10.1109/ECCE-Asia63110.2025.11111975
5. Ogata K. Modern control engineering. 4th ed. Upper Saddle River (NJ): Prentice Hall; 2002.
6. Dimoulias SC, Kontis EO, Papagiannis GK. Inertia estimation of synchronous devices: Review of available techniques and comparative assessment of conventional measurement-based approaches. Energies. 2022; 15(20):7767. https://doi.org/10.3390/en15207767
7. Zhang X, Wang Y, Blaabjerg F. Control of grid-forming VSCs: a perspective of adaptive fast/slow internal voltage source. IEEE Trans Power Electron. 2023; 38(10):12345-12357.